Supplementary Information (SI) for Materials Chemistry Frontiers.

Supporting Information

Boosting Fluorescence Efficiency of NIR-II Dyes for Multifunctional Fluorescence Imaging via Hydrogen Bonding

Liangyu Zheng[a], Weidan Na[b], Fan Gao[a], Changjin Ou[a*]*

[a]Institute of Advanced Materials and Flexible Electronics (IAMFE), School of Chemistry and Materials Science, Nanjing University of Information Science and Technology, Nanjing, JiangSu 210044, China.

[b]College of Chemistry and Chemical Engineering, Xuzhou University of Technology, Xuzhou, JiangSu 221111, China.

Corresponding author: ocj1987@163.com; wdna@xzit.edu.cn.

Experimental Section

Materials

All chemicals and reagents were purchased commercially from Shanghai Titan Technology Co., Ltd without further purification. All air and moisture sensitive reactions were carried out in flame-dried glassware under nitrogen protection. ^{1}H (400 MHz) and ^{13}C (100 MHz) nuclear magnetic resonance spectra were recorded on a JNM-ECZ400S/L1 spectrometer using tetramethylsilane (TMS) in $CDCl_3$ as an internal standard. MALDI-TOF mass spectra were performed on the Autoflex max LRF Matrix-Assisted Laser Desorption Ionization Time-of-Flight Mass Spectrometry.

Synthetic route of compound 2: A 50 mL two-necked round-bottom flask was charged with **1** (100 mg, 0.08 mmol), zinc powder (62 mg, 0.96 mmol) and NH_4Cl (26 mg, 0.48 mmol). After degassed by three vacuum pump cycles and backfilled with nitrogen, DCM (8 mL) and MeOH (4mL) were added, the mixture was stirred at room temperature for 5 h. The organic phase was filtered through a Celite pad and the solvent was evaporated under reduced pressure. The crude product was used without further purification.

Synthetic route of compound TP-OH: A 20 mL Schlenk flask was charged with **compound 2** and 1,2-bis(4-hydroxyphenyl)ethane-1,2-dione (29 mg, 0.12 mmol). After degassed by three vacuum pump cycles and backfilled with nitrogen, acetic acid (4 mL) was added and the mixture was stirred at 100 °C overnight. After cooling down to room temperature, water was added, and the mixture was washed with dichloromethane three times. The organic phase was combined and dried with anhydrous $MgSO_4$. After the removal of the solvent under reduced pressure, the crude product was purified by column chromatography on silica gel with dichloromethane and hexane mixture as eluent yielding **TP-OH** as a dark-green solid (62 mg, 57.8 %). **^{1}H NMR (400 MHz, $CDCl_3$)** δ 9.24 (s, 2H), 7.85 (d, *J* = 7.7 Hz, 2H), 7.57 (t, *J* = 9.1 Hz, 6H), 7.35 (d, *J* = 8.2 Hz, 8H), 7.29-7.20 (m, 4H), 7.10 (d, *J* = 8.3 Hz, 8H), 6.62 (d, *J* = 8.3 Hz, 4H), 2.55 (t, *J* = 7.8 Hz, 8H), 1.59 - 1.51 (m, 8H), 1.34 - 1.29 (m, 8H), 0.86 (t, *J* = 7.3 Hz, 12H); **^{13}C NMR (100 MHz, $CDCl_3$)** δ 161.5, 156.9, 152.2, 151.7, 151.4, 144.0, 143.7, 141.7, 139.8, 139.6, 138.2, 134.9, 134.5, 132.7, 130.6, 128.8, 128.6, 125.0, 124.0, 123.5, 122.2, 120.3, 115.1, 63.0, 35.4, 33.6, 22.6, 14.1. **MALDI-TOF-MS (m/z)** Calcd. 1352.43, found: 1353.44.

Synthetic route of compound TP-F: A 20 mL Schlenk flask was charged with **compound 2** and 1,2-bis(4-fluorophenyl)ethane-1,2-dione (30 mg, 0.12 mmol). After degassed by three vacuum pump cycles and backfilled with nitrogen, acetic acid (4 mL) was added and the mixture was stirred at 100 °C overnight. After cooling down to room temperature, water was added, and the mixture was washed with dichloromethane three times. The organic phase was combined and dried with anhydrous $MgSO_4$. After the removal of the solvent under reduced pressure, the crude product was purified by column chromatography on silica gel with dichloromethane and hexane mixture as eluent yielding **TP-F** as a yellow solid (46 mg, 42.7 %). **^{1}H NMR (400 MHz, $CDCl_3$)** δ 9.17 (s, 2H), 7.88 (d, *J* = 7.4 Hz, 2H), 7.74 - 7.66 (m, 4H), 7.59 (dd, *J* = 6.4, 1.9 Hz, 2H), 7.32 (d, *J* = 8.3 Hz, 8H), 7.29 - 7.25 (m, 5H), 7.09 (d, *J* = 8.5 Hz, 8H), 7.03 (t, *J* = 8.6 Hz, 4H), 2.56 (t, *J* = 7.8 Hz, 8H), 1.58 - 1.54 (m, 8H), 1.36 - 1.30 (m, 8H), 0.88 (t, *J* = 7.3 Hz, 12H); **^{13}C NMR (100 MHz, $CDCl_3$)** δ 161.8, 152.0, 151.6, 151.4, 144.1, 143.9, 141.7, 139.6, 139.2, 138.0, 134.7, 134.7, 133.9, 132.8(d, *J* = 8.2 Hz), 129.2, 128.6, 128.5, 125.0, 124.0, 123.7, 122.3, 120.8, 115.7 (d, *J* = 21.6 Hz), 63.0, 35.4, 33.6, 22.7, 14.1; **^{19}F NMR (376 MHz, $CDCl_3$)** δ -110.3 (s, 1F). **MALDI-TOF-MS (m/z)** Calcd. 1356.42, found: 1355.76.

Synthetic route of compound TP-OMe: A 20 mL Schlenk flask was charged with **compound 2** and 1,2-bis(4-methoxyphenyl)ethane-1,2-dione (32 mg, 0.12 mmol). After degassed by three vacuum pump cycles and backfilled with nitrogen, acetic acid (4 mL) was added and the mixture was stirred at 100 °C overnight. After cooling down to room temperature, water was added, and the mixture was washed with dichloromethane three times. The organic phase was combined and dried with anhydrous $MgSO_4$. After the removal of the solvent under reduced pressure, the crude product was purified by column chromatography on silica gel with dichloromethane and hexane mixture as eluent yielding **TP-OMe** as a yellow solid (48 mg, 43.8 %). **^{1}H NMR (400 MHz, $CDCl_3$)** δ 9.22 (s, 2H), 7.88 (d, *J* = 7.4 Hz, 2H), 7.76 (d, *J* = 8.7 Hz, 4H), 7.61 (d, *J* = 8.3 Hz, 2H), 7.35 (d, *J* = 8.2 Hz, 8H), 7.30-7.24 (m, 4H), 7.11 (d, *J* = 8.3 Hz, 8H), 6.90 (d, *J* = 8.8 Hz, 4H), 3.87 (s, 6H), 2.58 (t, *J* = 7.8 Hz, 8H), 1.62 - 1.54 (m, 8H), 1.39 - 1.35 (m, 8H), 0.91 (d, *J* = 7.3 Hz, 12H); **^{13}C NMR (100 MHz, $CDCl_3$)** δ 161.6, 161.0, 152.4, 151.7, 151.5, 144.0, 143.5, 141.6, 139.7, 139.5, 138.3, 134.8, 134.8, 132.5, 130.7, 128.8, 128.6, 128.5, 125.0, 124.0, 123.5, 122.2, 120.4, 113.9, 63.0, 55.4, 35.4, 33.6, 22.6, 14.1. **MALDI-TOF-MS (m/z)** Calcd. 1380.46, found: 1380.84.

Synthetic route of compound TP-Acr: A 20 mL Schlenk flask was charged with compound **TP-OH** (27 mg，0.02 mmol), triethylamine (14 μL，0.1 mmol), acryloyl chloride (36 mg，0.40 mmol) and dichloromethane (5 mL), the resulting mixture was stirred at room temperature overnight. After the addition of deionized water, the mixture was extracted by dichloromethane. The solvent was removed under reduced pressure, the crude product was purified by column chromatography on silica gel with dichloromethane and hexane mixture as eluent yielding **TP-Acr** as a dark solid (25 mg, 85.7 %). **^{1}H NMR (400 MHz, $CDCl_3$)** δ 9.17 (s, 2H), 7.85 (t, *J* = 7.3 Hz, 6H), 7.59 (d, *J* = 6.5 Hz, 2H), 7.35 - 7.29 (m, 8H), 7.28 - 7.21 (m, 8H), 7.09 (d, *J* = 8.5 Hz, 8H), 6.68 (d, *J* = 17.3 Hz, 2H), 6.38 (dd, *J* = 17.4, 10.4 Hz, 2H), 6.08 (d, *J* = 10.4 Hz, 2H), 2.56 (t, *J* = 7.8 Hz, 8H), 1.60 - 1.52 (m, 8H), 1.36 - 1.32 (m, 8H), 0.88 (d, *J* = 7.4 Hz, 12H); **^{13}C NMR (100 MHz, $CDCl_3$)** δ 164.2, 161.8, 151.9, 151.9, 151.7, 151.6, 144.1, 143.9, 141.6, 139.6, 139.3, 138.1, 135.4, 134.8, 134.7, 133.1, 132.0, 129.1, 128.6, 128.5, 128.0, 125.0, 124.0, 123.6, 122.3, 121.7, 121.0, 63.0, 35.4, 33.6, 22.7, 14.1. **MALDI-TOF-MS (m/z)** Calcd. 1460.45, found: 1460.82.

Theoretical calculation

All-electron DFT calculations have been carried out by the ORCA quantum chemistry software[1] (Version 6.0.0). For geometry optimization calculations, the BLYP functional and def2-SVP basis set were adopted. The singlet point energy calculations

were performed with B3LYP functional and def2-SVP basis set. The DFT-D3 dispersion correction with BJ-damping[2] was applied to correct the weak interaction to improve the calculation accuracy. The nature of noncovalent interaction was studied by using IGM (Independent Gradient Model) method through Multiwfn software[3]. The visualization of IGM and orbitals were rendered by VMD[4]

Preparation of nanoparticles

TP-OH, TP-OMe, TP-F and TP-Acr were each dissolved in tetrahydrofuran along with eight times the mass of Pluronic F127, and the solutions were rapidly injected into deionized water with high-speed stirring using a microsyringe. The tetrahydrofuran was removed using a rotary evaporator to obtain the corresponding aqueous solutions of nanoparticles (NPs).

Fluorescence quantum yield

The absorption and fluorescence spectra of NPs were measured with a Shimadzu UV-Vis-NIR spectroscopy (UV-3600 Plus) and an Edinburgh Instrument spectrofluorometer (FLS1000), respectively. The average particle sizes of NPs were determined by a NICOMP particle sizer instrument (Z3000 plus) equipment at room temperature. The absorption coefficients of molecules and NPs were calculated based on the above calibration curves and Beer-Lambert Law. To measure the QY of molecules and NPs, the samples and FT-BBT were dispersed in water and toluene at various concentrations, respectively. The fluorescence intensity of these samples was calculated from the greyscale values of the fluorescence images acquired by Image J. Fluorescence images were obtained using a Series III 900/1700-M fluorescence imager under 808 nm excitation (10 mW cm^{-2}, 20 ms) with 900LP filter. The integrated area of fluorescent profile was plotted against concentration to obtain the slope. QYs was calculated in the following manner:

$$QYs_{sample} = QYs_{FT-BBT}\frac{Slope_{sample}\ n_{sample}^{2}}{Slope_{FT-BBT}n_{FT-BBT}^{2}}$$

Where QYs_{FT-BBT} in toluene is 19%; the refractive index (n_{water} and $n_{Toluene}$) is 1.3330 and 1.4967, respectively.

Photothermal effect

The photostability of TP-OH NPs in H_2O was explored by monitoring its photothermal effect during five laser on/off cycles with 808 nm laser irradiation (0.5 mW cm^{-2}). The aqueous solution of TP-OH NPs (100 μg mL^{-1}) was exposed to an 808 nm laser at 0.5 W cm^{-2} for 10 min (laser on), and then cooled naturally for 10min (laser off). This laser on/off cycle was repeated five times. Furthermore, aqueous solutions of TP-OH, TP-OMe, TP-F and TP-Acr NPs were irradiated at 808 nm laser irradiation (0.5 W cm^{-2}) for 15 min. A portable infrared thermometer was used to record the temperature at 20 s intervals during these procedures. The photothermal conversion efficiency was calculated by the following equation:

$$PCE = \frac{\frac{m_D C_D}{\tau_s}\Delta T_{max} - Q_S}{I(1-10^{-A})}$$

Where ΔT_{max} is the temperature change of NPs aqueous solution at the maximum steady-state temperature, τ_s is the sample-system time constant, m_D and C_D are the mass and heat capacity (4.2 J g^{-1}) of the H_2O used as the solvent, Q_S is the heat associated with light absorption by the solvent. The I is the laser power, A is absorbance of the NPs aqueous solution at 808 nm.

MTT assay

The metabolic viability of 4T1 cells was evaluated by Cell Viability Kit 3-(4,5- dimethylthiazol-2-yl)-2,5-diphenyltetrazolium bromide (MTT) assay. 4T1 cells were incubated in DMEM medium containing 10% FBS and 1% antibiotics (penicillin–streptomycin, 10000 U/mL). All cells were cultured at 37 °C in a humidified atmosphere containing 5% CO_2 and 95% air. The cells were seeded in two 96-well plates at a density of 5 × 10^3 cells/well labelled with No Laser and Laser. After culture in the incubator for 24 h, the old medium was replaced with 100 μL of TP-OH NPs solutions at concentrations of 0, 10, 20, 30, 40, 50, 60, 70, 80, 90 μg mL^{-1}. Upon incubation for another 24 h, 20 μL of MTT solution was added and incubated in 37 °C for 4 hours to evaluate the dark cytotoxicity of TP-OH NPs. Furthermore, cells were also exposed to 808 nm laser irradiation (0.5 W cm^{-2}) for 5 min and incubated for 20 h for photothermal cytotoxicity study under the same experimental conditions. Then 150 μL DMSO were added into each well, the absorbance at 490 nm from each well was recorded by a microplate reader (Varioskan LUX). The cell viability was expressed by the ratio of absorbance from the cells treated with NPs to that of the cells incubated with culture medium only.

Live-dead co-staining

4T1 cells were added to 24-well plates (5 × 10^3 cells/well). After incubation for 24 h, the cells were incubated with TP-OH NPs at a concentration of 0 and 100 μg mL^{-1} with or without the laser at each concentration under two conditions and the cells

were continuously incubated for 6 h. Subsequently, the cells were rinsed twice with PBS. Afterwards, the 4T1 cells were stained using a calcein AM/PI Detection Kit. The live and dead cells were then imaged under a fluorescence microscope (NIB900).

Tumor model

The female Balb/c mice (14-18 g weight, five weeks aged) were purchased from Comparative Medicine Centre of Yangzhou University. All animal experiments were approved and guided by the Zhejiang Provincial People's Hospital, Affiliated People's Hospital, Hangzhou Medical College, in compliance with the relevant laws and institutional guidelines. The 4T1 cells were inoculated into the left rear leg of the mice with 50 μL of PBS containing 4×10^6 cells. When the tumor volumes approached 100-150 mm^3, the mice were used to carry out the following *in vivo* experiments.

NIR-II fluorescence imaging

Nude mice were anaesthetised using a gas anaesthesia system after injection of TP-OH NPs (2 mg mL^{-1}, 150 μL) via a tail vein. The fluorescence signal from blood vessels was detected and recorded under a NIR-II imaging instrument equipped with an 808 nm laser (1100 nm long-pass filter, 20 mW cm^{-2}, and 200 ms exposure time).

The hair on the back of T1 tumor-bearing BALB/c mice was removed before imaging tests were performed. After the injection of TP-OH NPs (2 mg mL^{-1}, 150 μL) via a tail vein, BALB/c mice were anesthetized using a gas anesthesia system. The fluorescence signal from the tumor site at various times was detected and recorded under a NIR-II imaging instrument equipped with an 808 nm laser (1000 nm long-pass filter, 20 mW cm^{-2}, and 100 ms exposure time). The fluorescence intensity of these images was calculated from the greyscale values of the fluorescence images acquired by Image J.

The hair on the leg of BALB/c mice was removed before lymphatic imaging tests were performed. After the intradermal injection of TP-OH NPs (40 μL，0.15 μmol mL^{-1}) into the footpad, BALB/c mice were anesthetized using a gas anesthesia system. The fluorescence signal from the popliteal lymph node site at various times was detected and recorded under a NIR-II imaging instrument equipped with an 808 nm laser (900 nm long-pass filter, 100 mW cm^{-2}, and 100 ms exposure time). The fluorescence intensity of these images was calculated from the greyscale values of the fluorescence images acquired by Image J.

BALB/c mice were shaved of their abdominal hair before gastrointestinal imaging tests were performed. After oral gavage of TP-OH NPs to the mice using a feeding needle, the mice were anesthetized using a gas anesthesia system. The fluorescence signal from the popliteal lymph node site at various times was detected and recorded under a NIR-II imaging instrument equipped with an 808 nm laser (1100 nm long-pass filter,25 mW cm^{-2}, and 200 ms exposure time). The fluorescence intensity of these images was calculated from the greyscale values of the fluorescence images acquired by Image J.

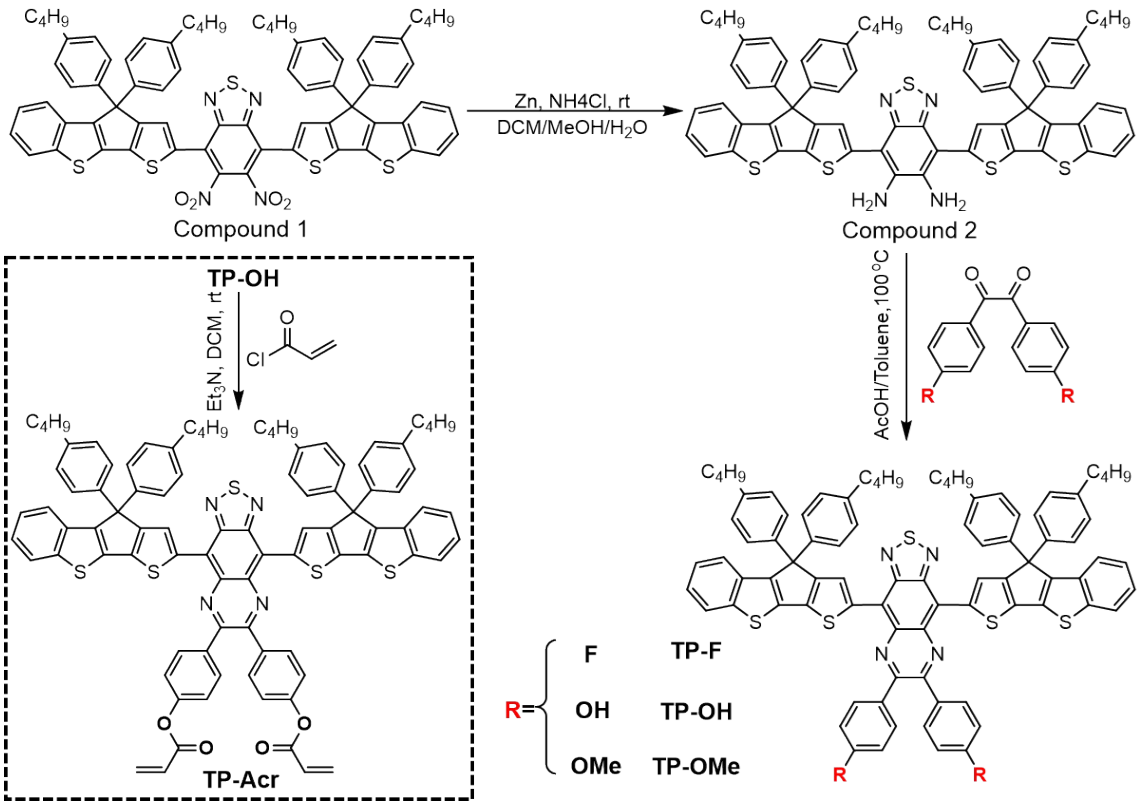

Scheme S1. The synthetic routes of TP-OH, TP-F, TP-OMe and TP-Acr.

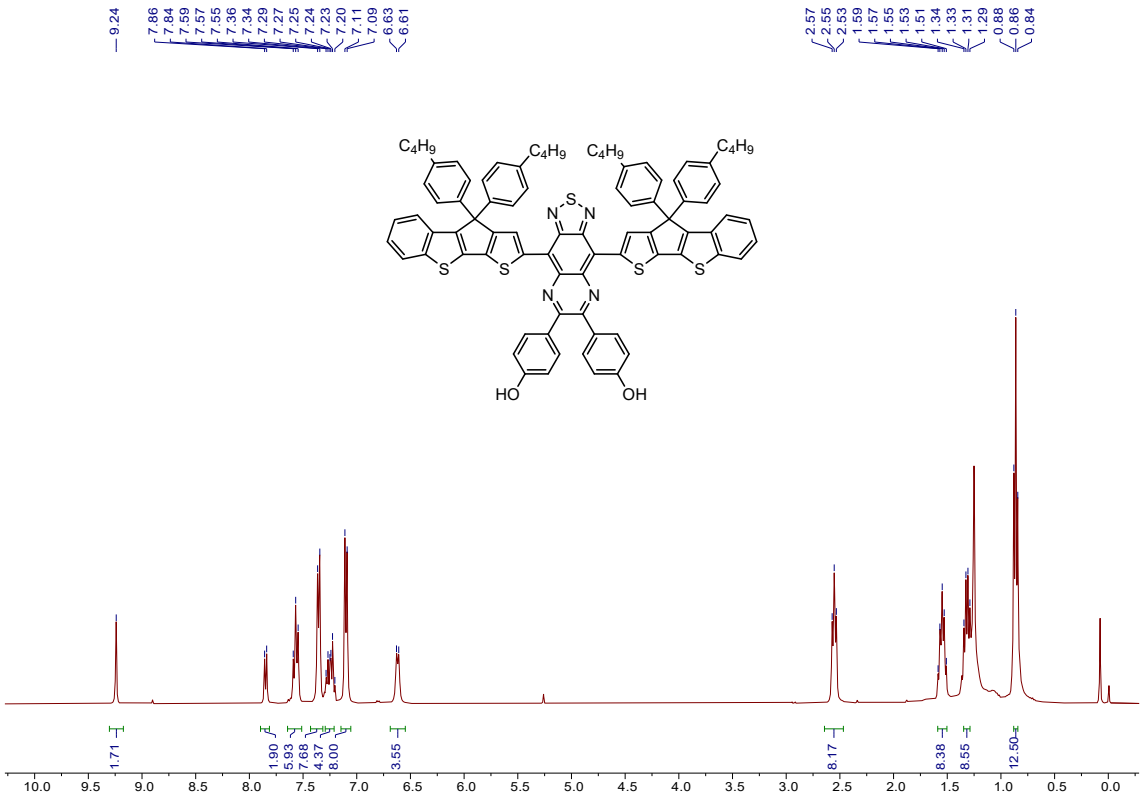

Figure S1 ^{1}H NMR spectrum of compound TP-OH.

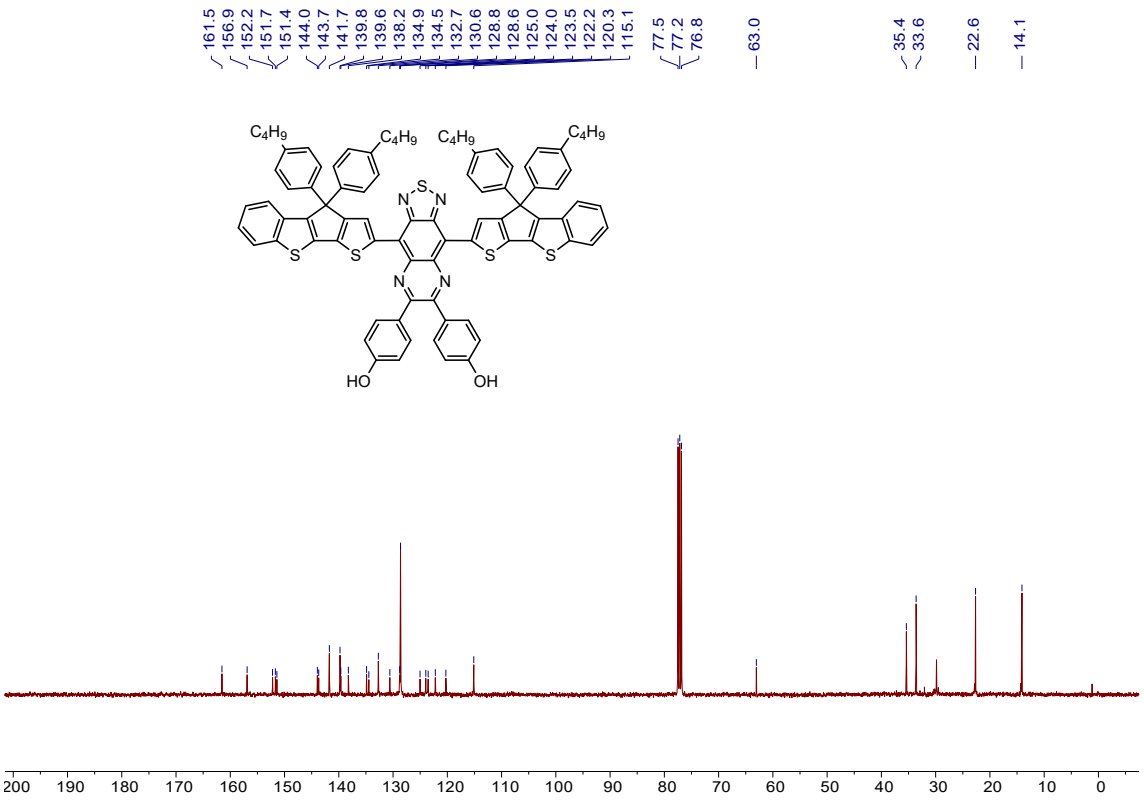

Figure S2 ^{13}C NMR spectrum of compound TP-OH.

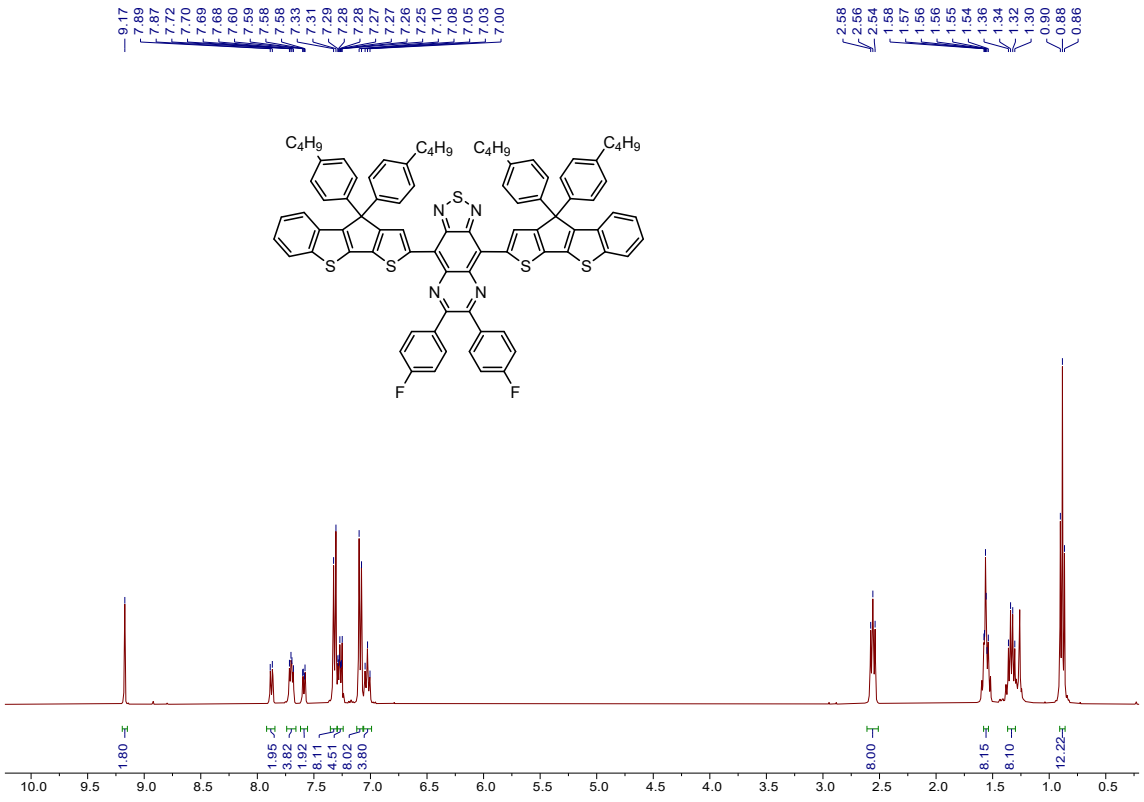

Figure S3 ^{1}H NMR spectrum of compound TP-F.

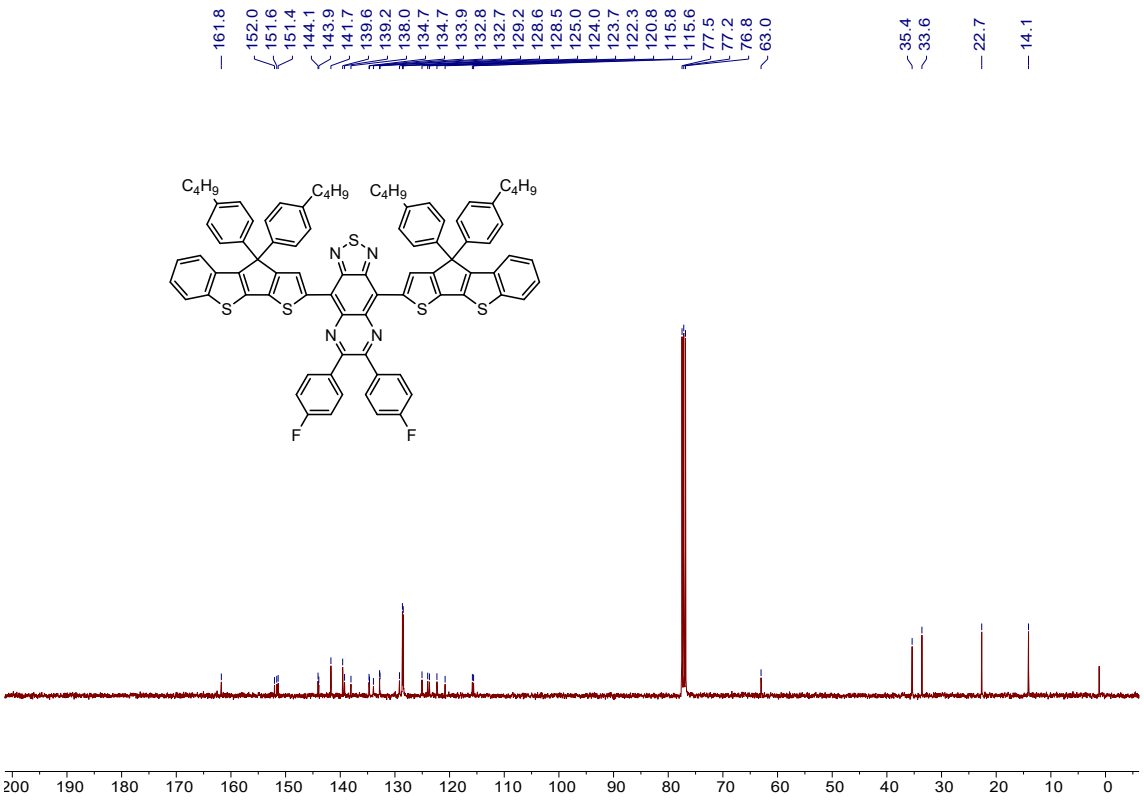

Figure S4 ^{13}C NMR spectrum of compound TP-F.

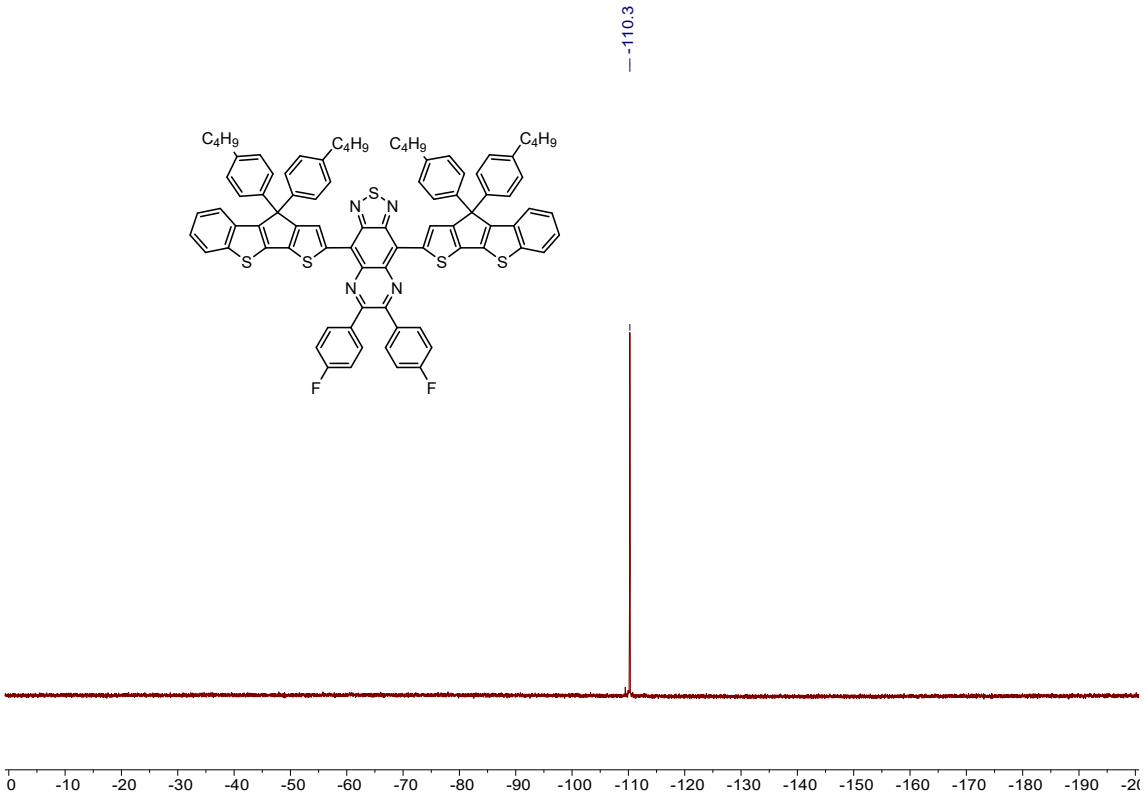

Figure S5 ^{19}F NMR spectrum of compound TP-F.

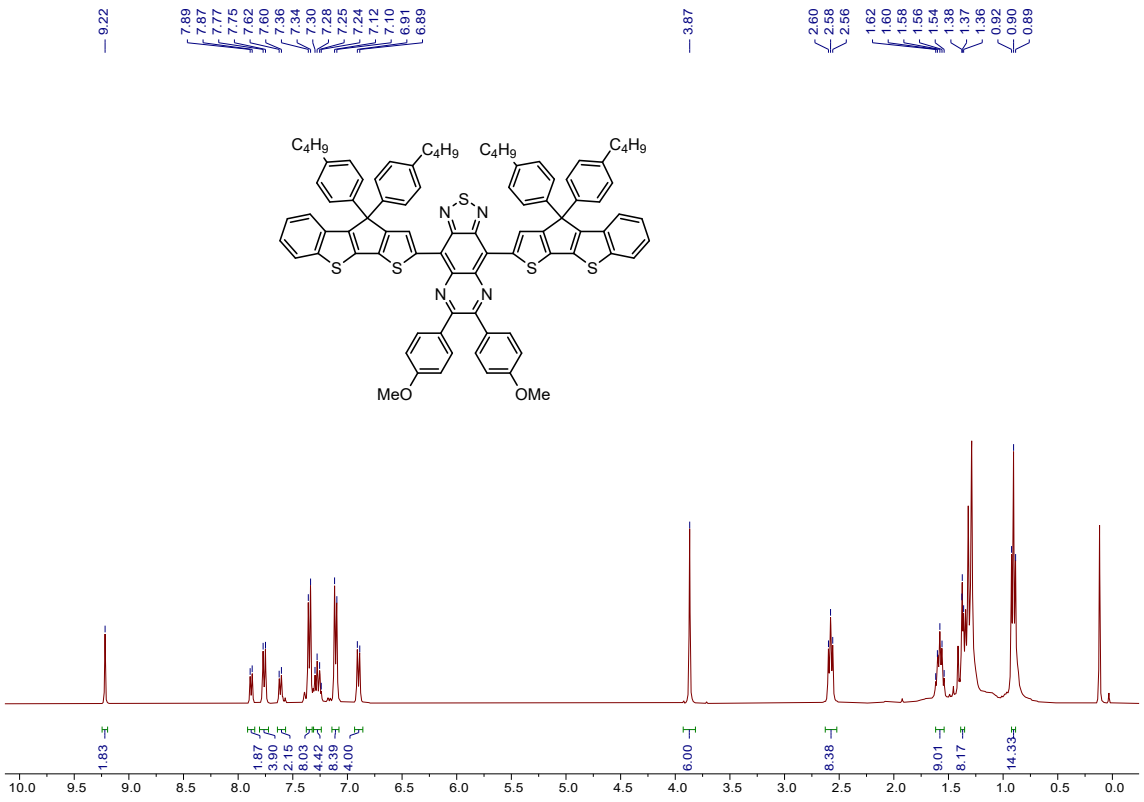

Figure S6 ^{1}H NMR spectrum of compound TP-OMe.

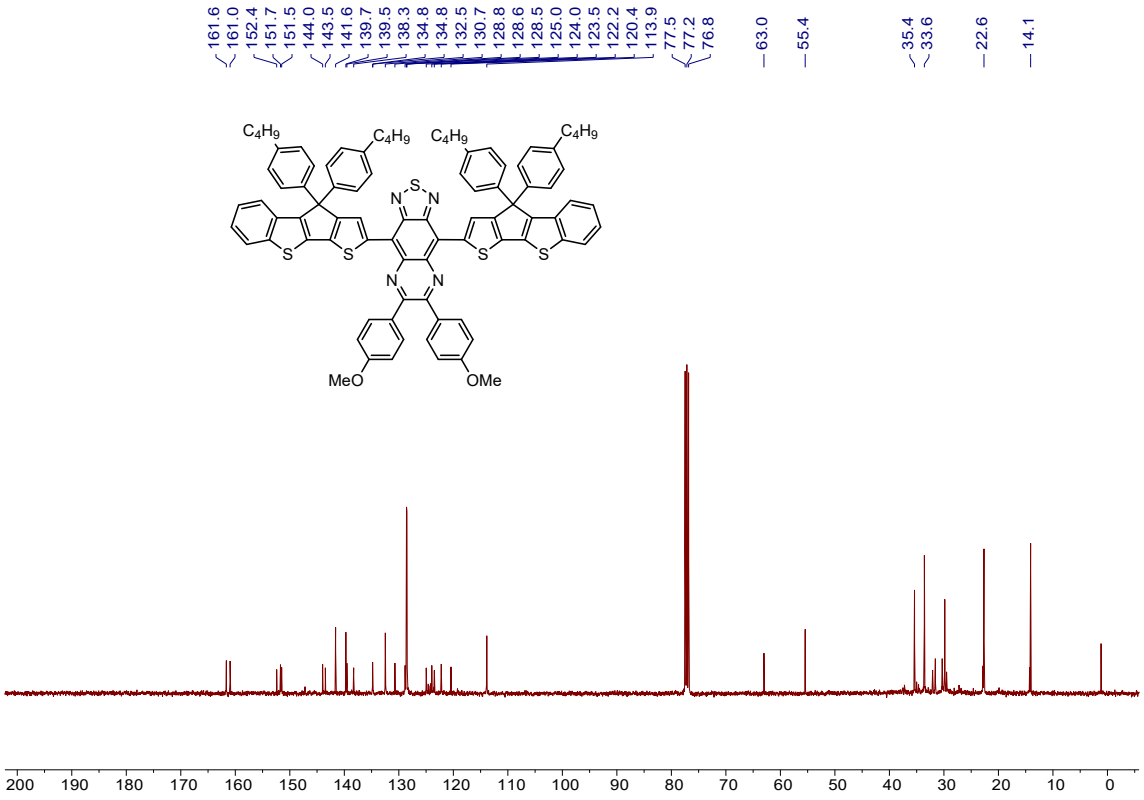

Figure S7 ^{13}C NMR spectrum of compound TP-OMe.

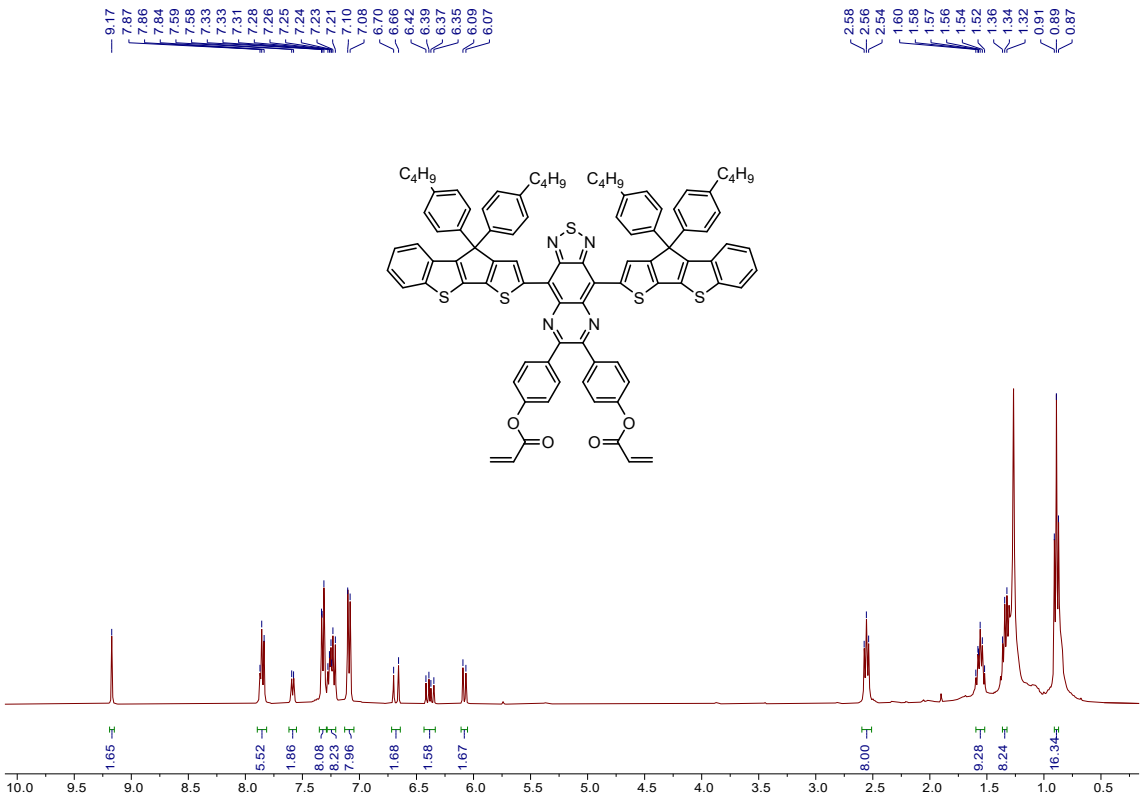

Figure S8 ^{1}H NMR spectrum of compound TP-Acr.

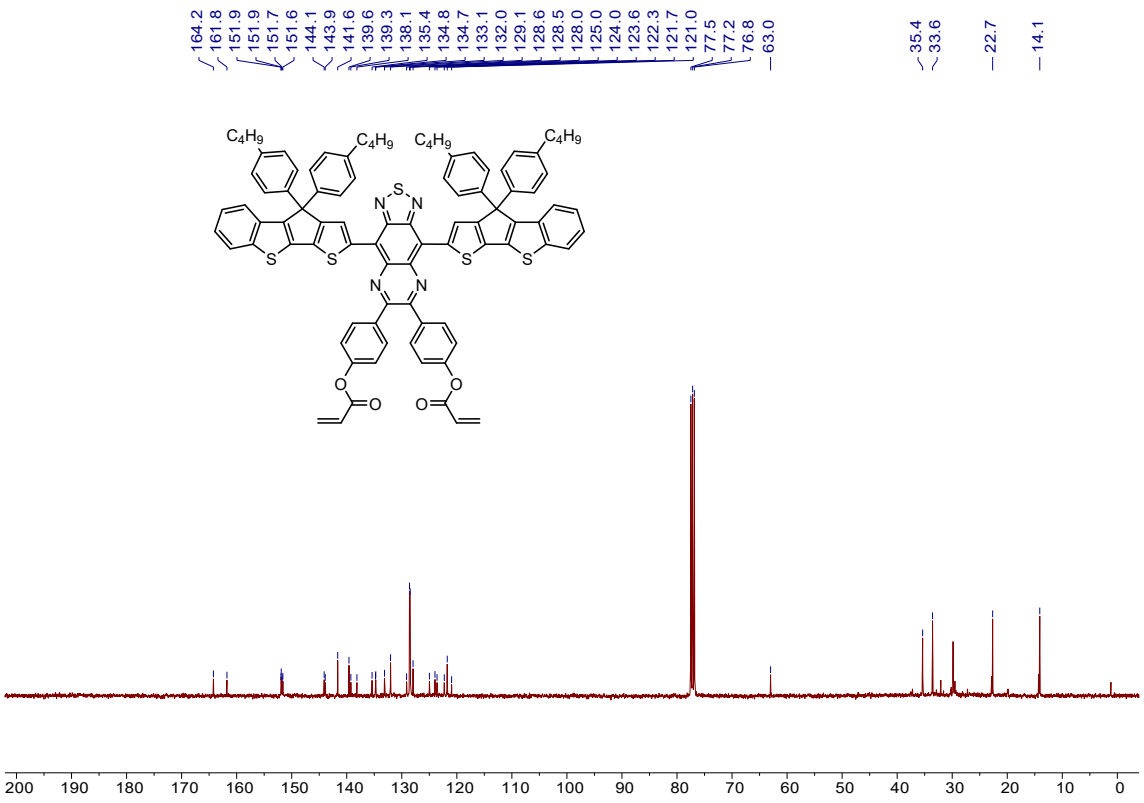

Figure S9 ^{13}C NMR spectrum of compound TP-Acr

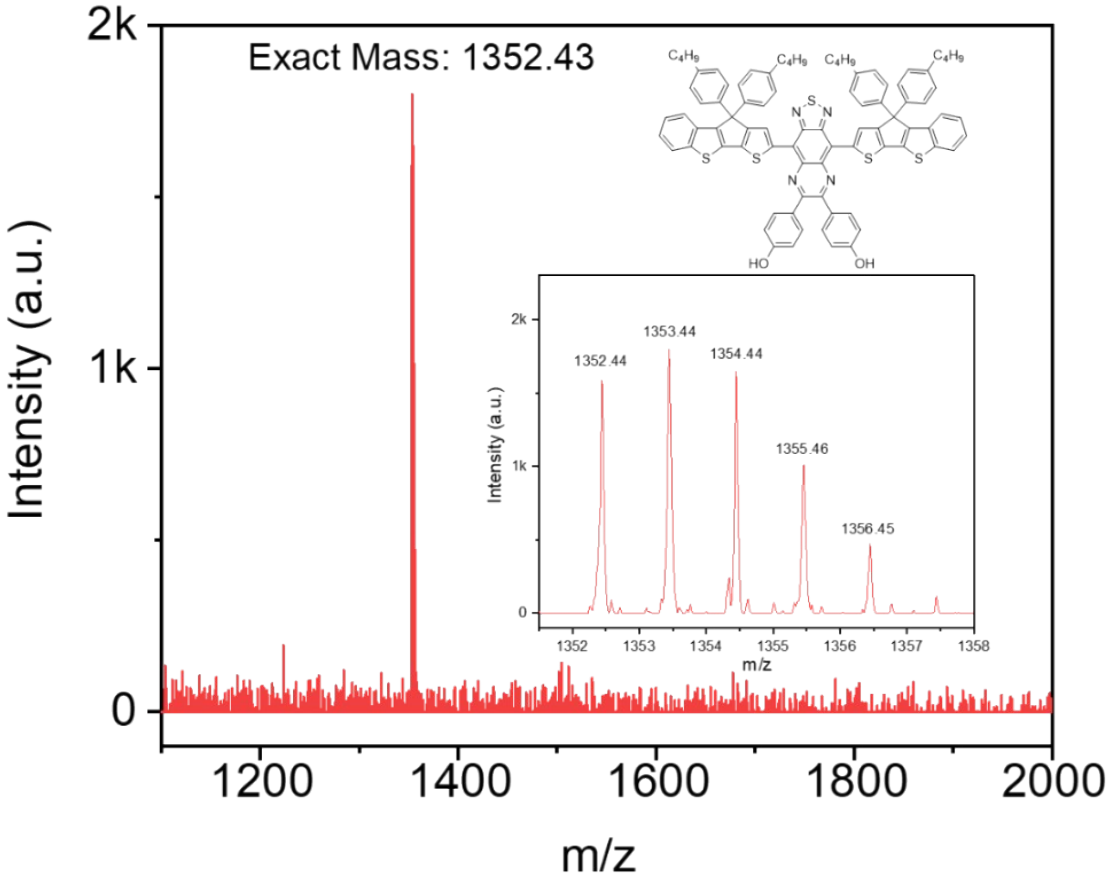

Figure S10. MALDI-TOF-MS spectrum of compound TP-OH.

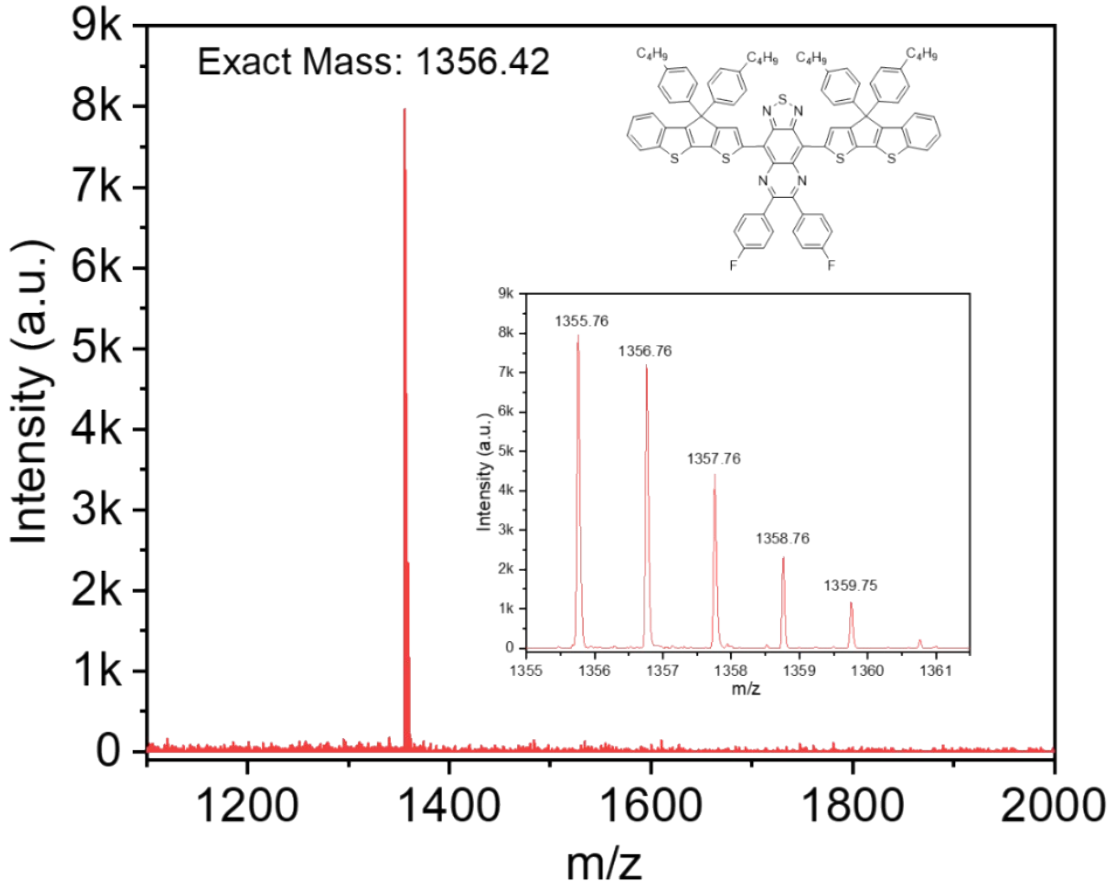

Figure S11. MALDI-TOF-MS spectrum of compound TP-F.

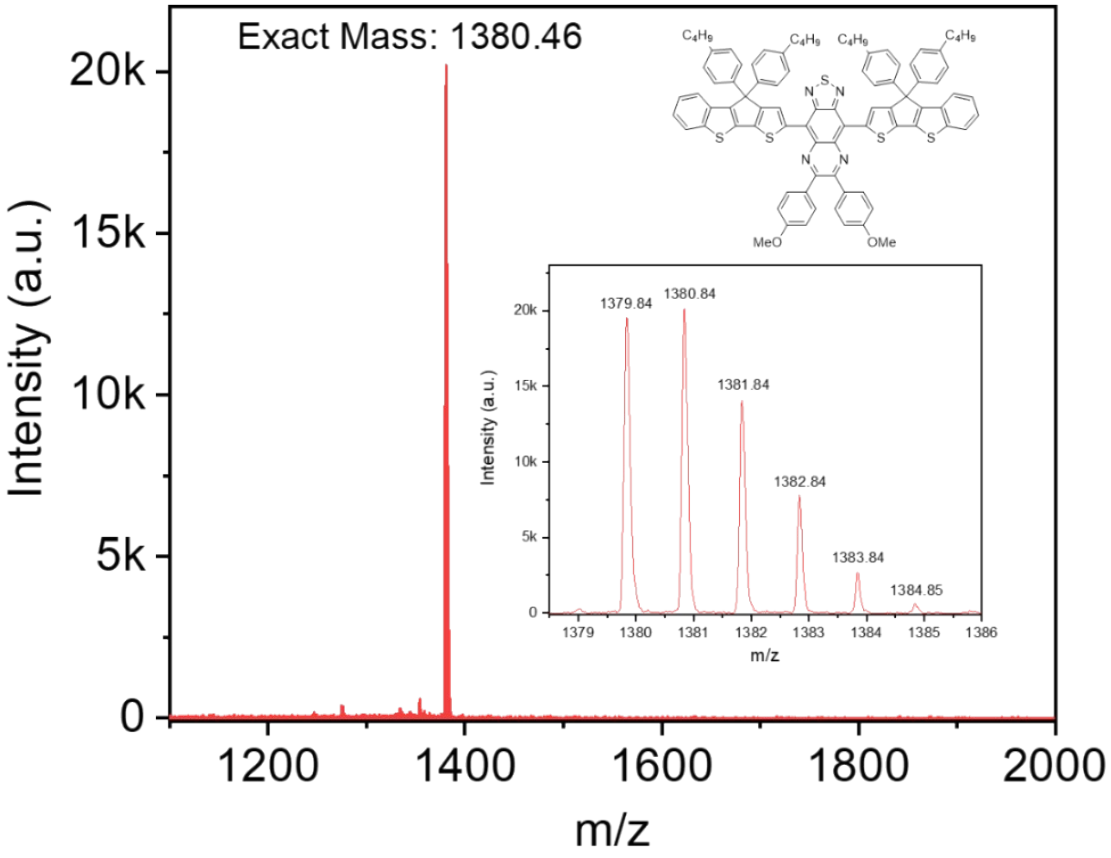

Figure S12. MALDI-TOF-MS spectrum of compound TP-OMe.

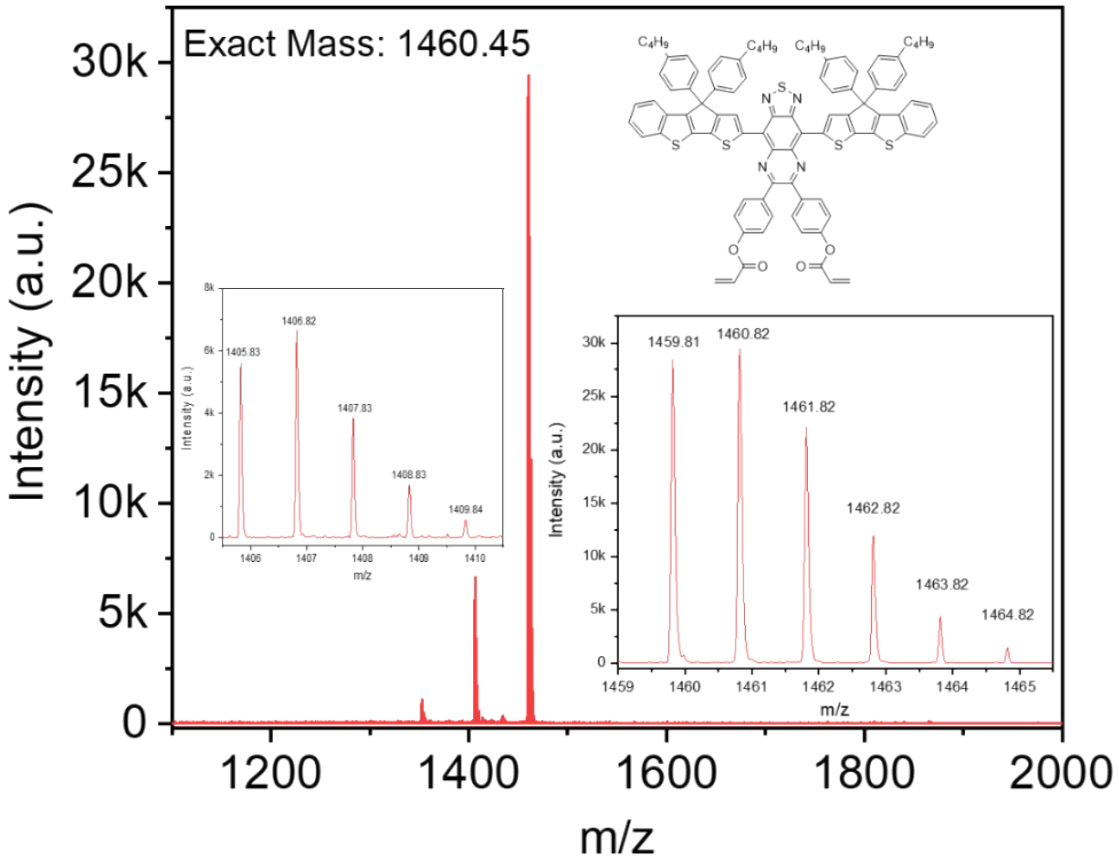

Figure S13. MALDI-TOF-MS spectrum of compound TP-Acr.

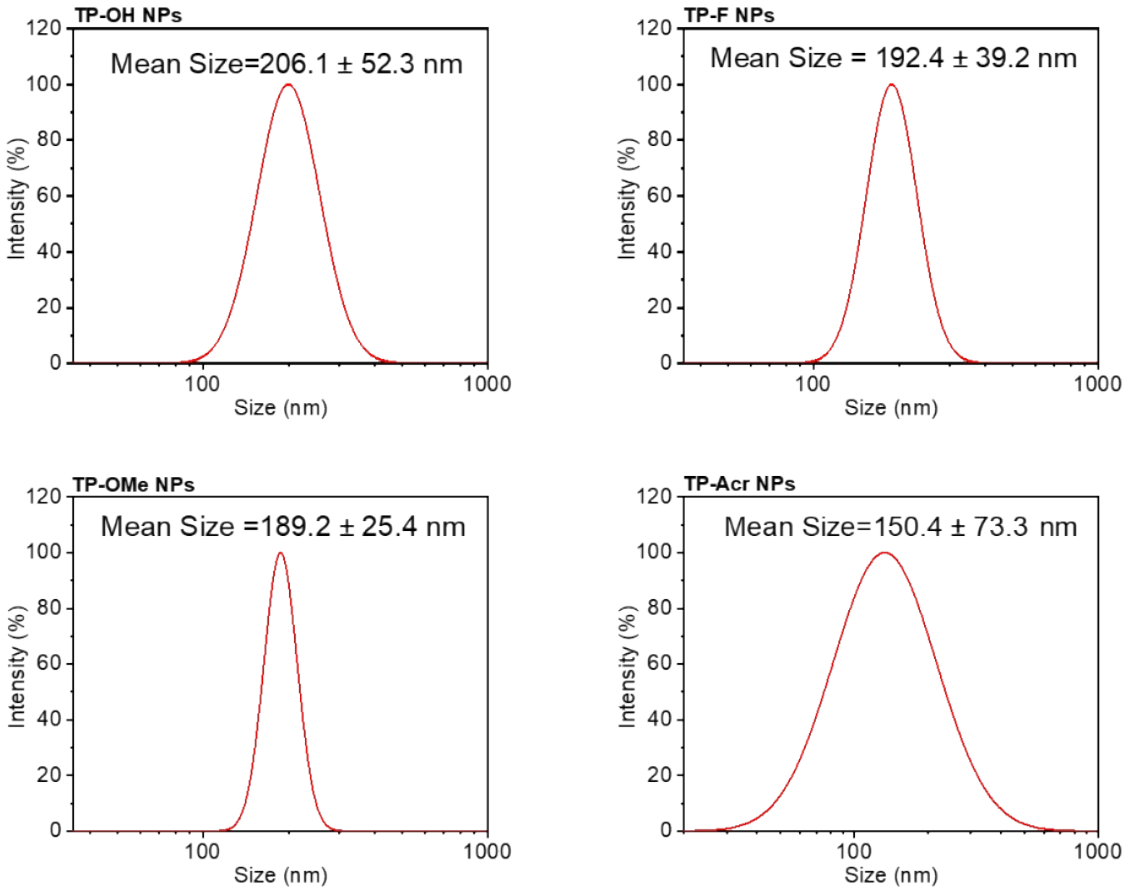

Figure S14. Dynamic light scattering results of TP-OH, TP-OMe, TP-F and TP-Acr NPs.

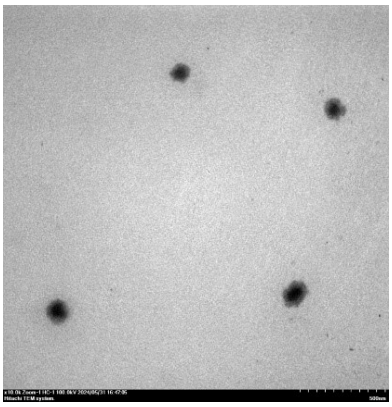

Figure S15. Transmission electron microscopy (TEM) image of TP-OH NPs.

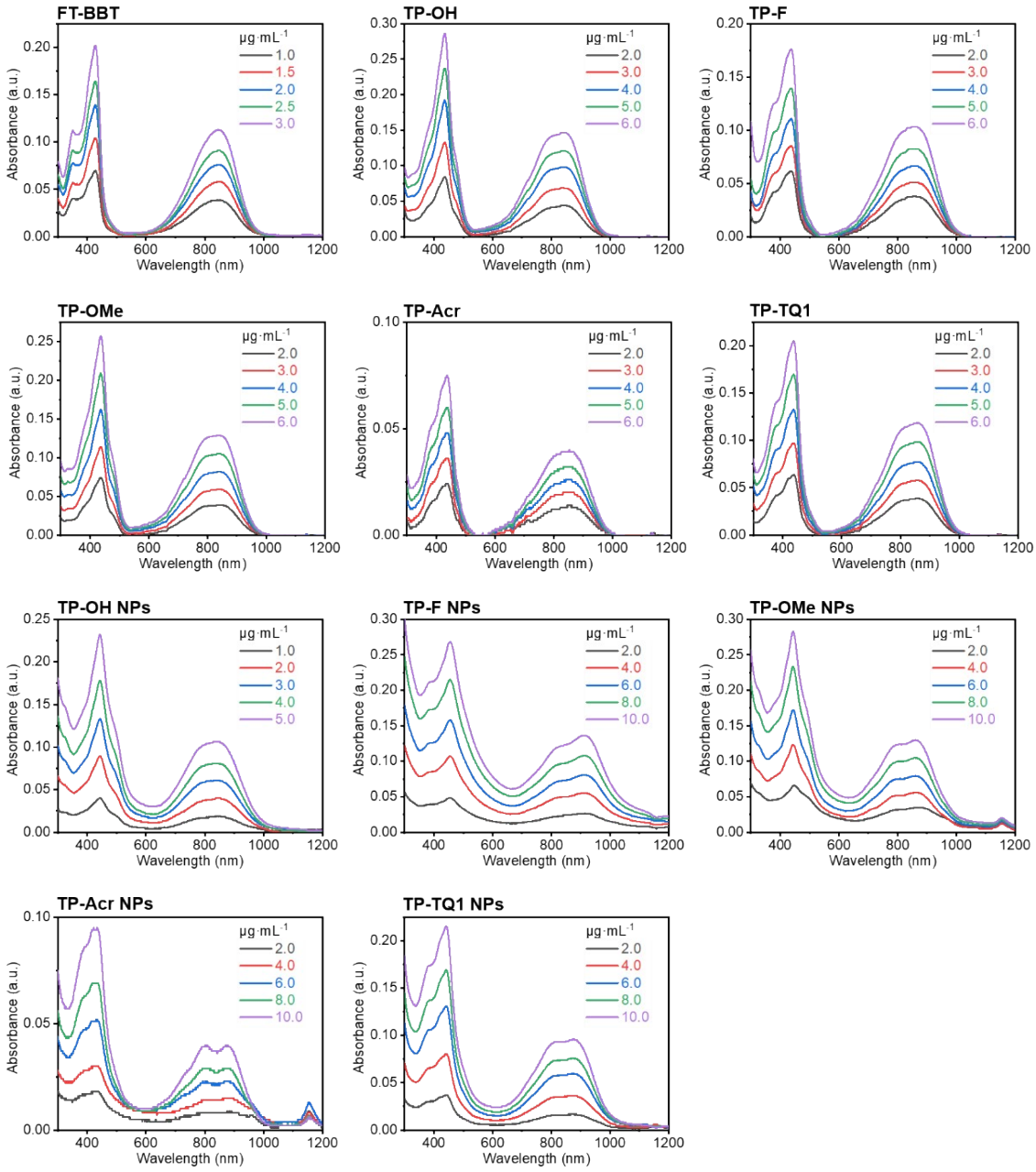

Figure S16. Absorption spectra of TP-OH, TP-OMe, TP-F, TP-Acr, TP-TQ1 and FT-BBT in toluene with different concentrations, respectively; Absorption spectra of TP-OH, TP-OMe, TP-F, TP-Acr and TP-TQ1 NPs in H_2O with different concentrations, respectively.

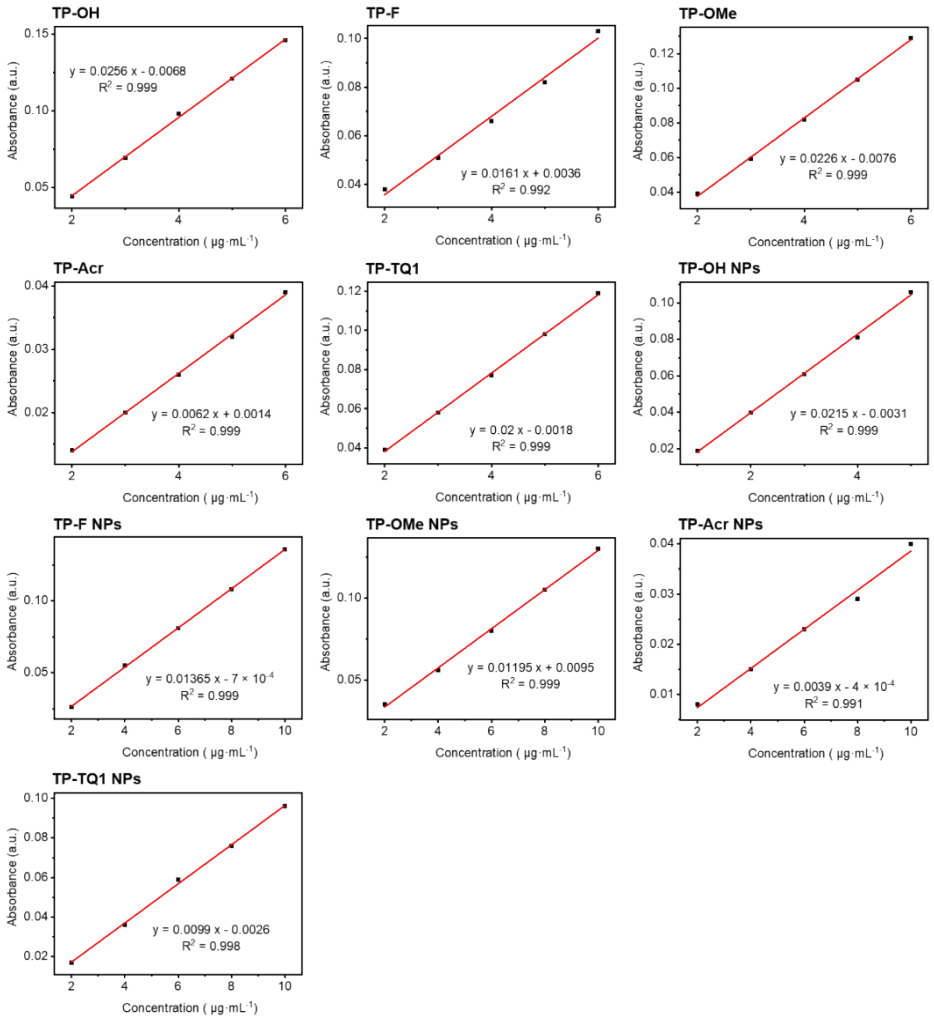

Figure S17. Linear-fitted slopes of absorption values at the maximum absorption peaks of TP-OH, TP-OMe, TP-F, TP-Acr and TP-TQ1 in toluene versus the corresponding concentration values; Linear-fitted slopes of the integrated fluorescence intensities of TP-OH, TP-OMe, TP-F, TP-Acr and TP-TQ1 NPs in H_2O versus the corresponding concentration values.

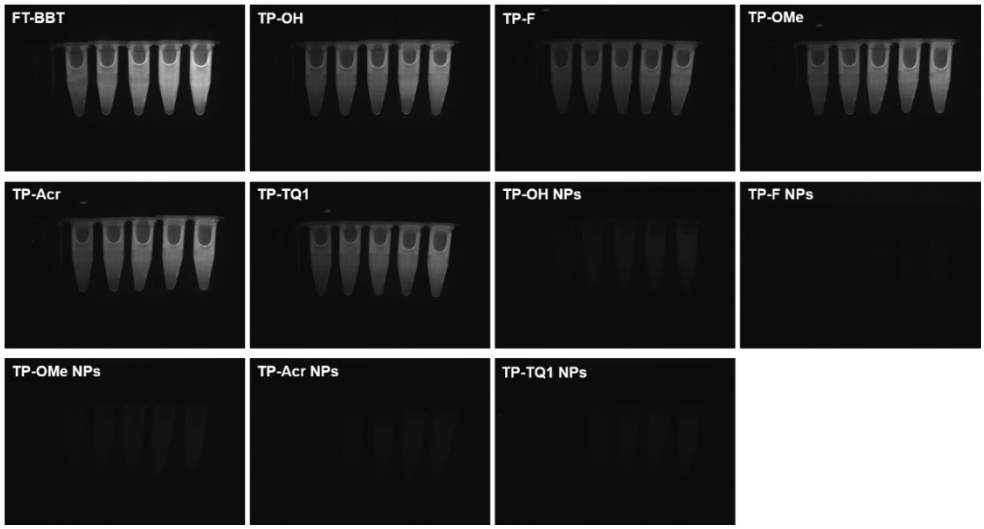

Figure S18. Fluorescence images of TP-OH, TP-OMe, TP-F, TP-Acr, TP-TQ1 and FT-BBT in toluene with different concentrations (The gradient concentration values are the same as in Figure S17) under 808 nm excitation (900 LP filter, 10 mW cm^{-1}, exposure time 20 ms), respectively; Fluorescence images of TP-OH, TP-OMe, TP-F, TP-Acr and TP-TQ1 NPs in H_2O with different concentrations The gradient concentration values are the same as in Figure S17) under 808 nm excitation (900 LP filter, 10 mW cm^{-1}, exposure time 20 ms), respectively.

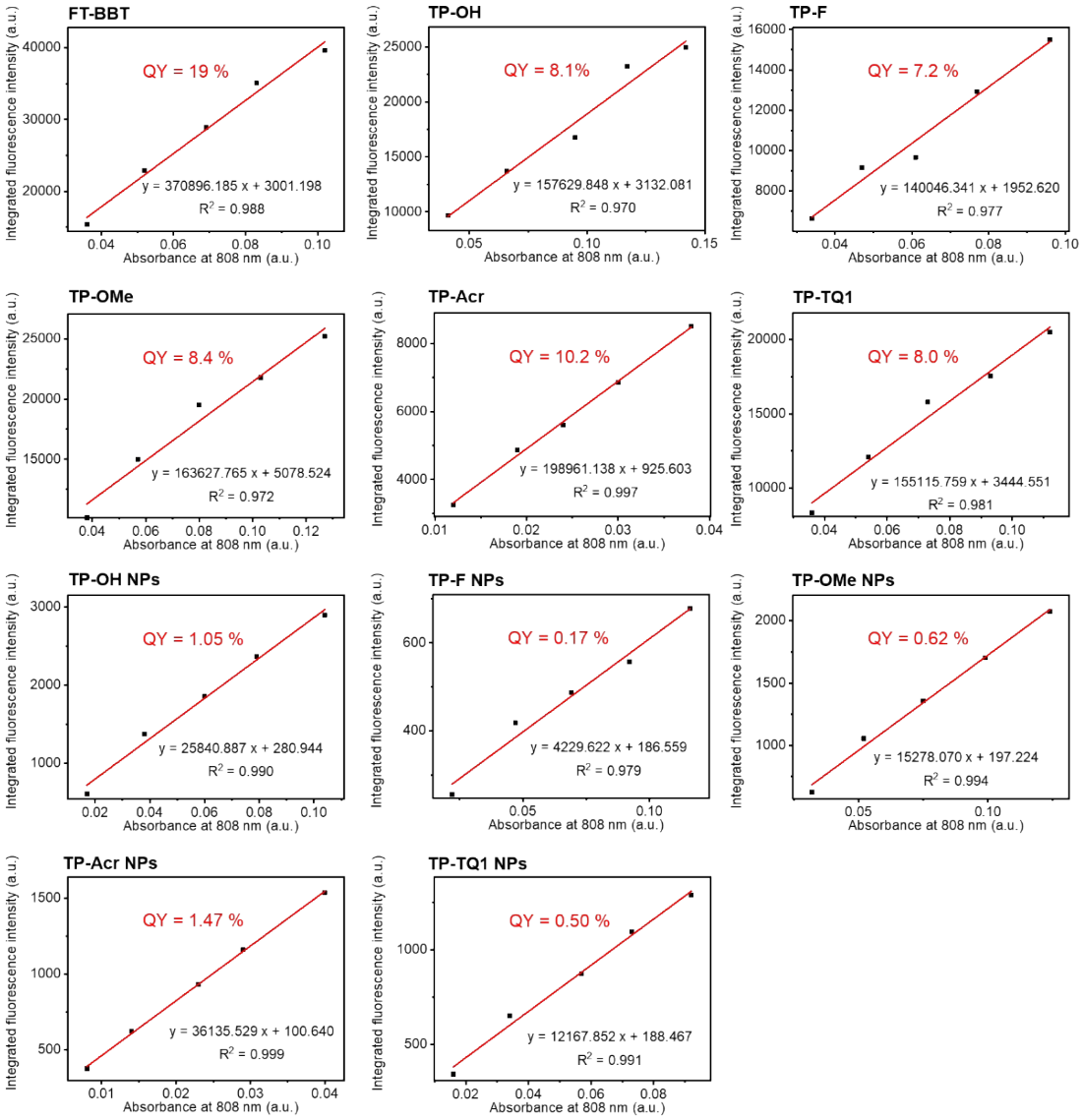

Figure S19. Determination of QY. Linear-fitted slopes of the integrated fluorescence intensities of TP-OH, TP-OMe, TP-F, TP-Acr, TP-TQ1 and FT-BBT in toluene above 900 nm versus the corresponding absorption values at 808 nm; Linear-fitted slopes of the integrated fluorescence intensities of TP-OH, TP-OMe, TP-F, TP-Acr and TP-TQ1 NPs in H_2O above 900 nm versus the corresponding absorption values at 808 nm.

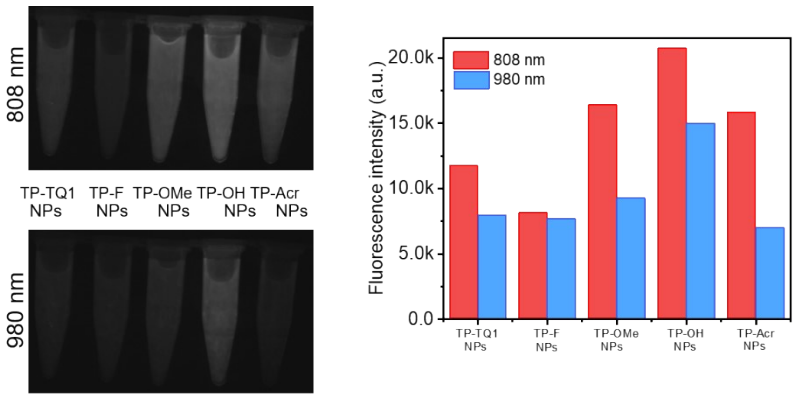

Figure S20. Fluorescence images and corresponding intensity of TP-OH, TP-OMe, TP-F and TP-Acr NPs in aqueous solution with the same concentration (100 mg mL^{-1}) under 808 (power fluence: 10 mW cm^{-2}, exposure time: 50 ms, 1000 nm long-pass filter) and 980 (power fluence: 9 mW cm^{-2}, exposure time: 50 ms, 1000 nm long-pass filter) nm laser excitation with different filters.

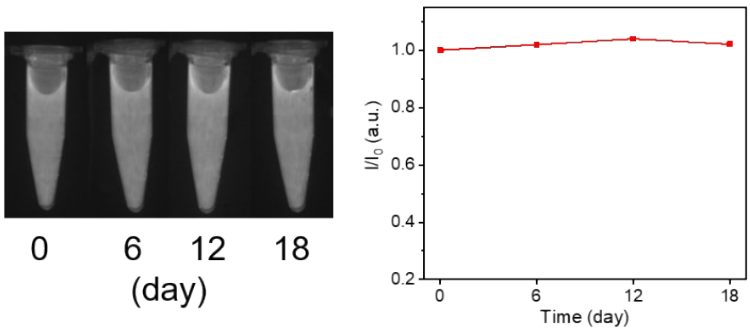

Figure S21. The change of fluorescence intensity of TP-OH NPs over 18 days in deionized water.

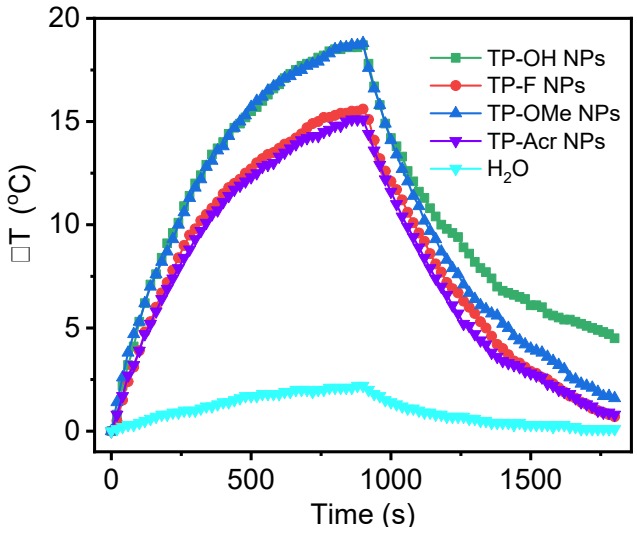

Figure S22. Photothermal effect of the TP-OH, TP-OMe, TP-F, TP-Acr NPs and H_2O under 808 nm laser irradiation (c = 100 μg mL^{-1}, *P* = 0.5 W cm^{-2}).

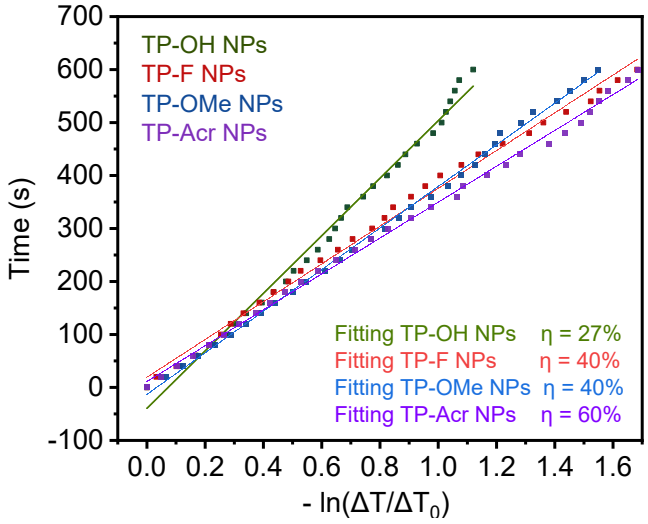

Figure S23. Plot of time versus -LN(θ) of NPs, θ ($\Delta T/\Delta T_0$) is driving force of temperature.

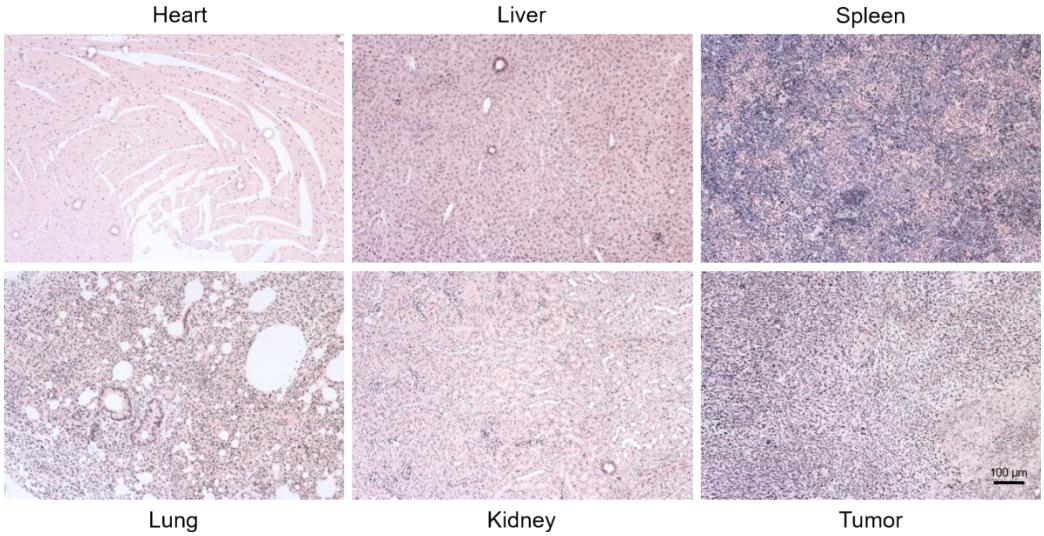

Figure S24. Hematxylin-eosin staining of the main organs and tumor f from mice sacrificed 36 hours after intravenous injection of TP-OH NPs. Scale bar: 100 μm.

Table S1. Optical properties of the TQ-based molecules and NPs

	$\lambda_{abs,max}$[a] (nm)	$\lambda_{em,max}$[b] (nm)	Stokes shift (nm)	ε [c] (L mol^{-1} cm^{-1})	QY[d] (%)	Ref.
TQ-BPN dots	630	810	180	/	2.8	5
DPTQ-PTZ NPs	639	928	289	/	0.059	6
DPTQ-PhPTZ	646	926	280	8700	0.092	7
TTQ-DP NPs	648	896	248	16000	9.88	8
DPTQ-PhPXZ	655	911	256	9700	0.14	7
MGNPs	681	915	234	/	1.3	9
TTQP NPs	711	1050	339	32900	0.47	8
TTQT NPs	730	1152	422	25700	2.6	10
TTQ-F@NPs	733	1060	327	/	/	11
TTQ-SF@NPs	735	1037	302	7941	0.84	12
TBP-b-DFA NPs	740	909	169	4100	/	13
TTQPL NPs	745	1092	347	31200	1.5	10
TTQiT NPs	755	1102	347	36600	3.7	10
FT-TQT (H2O)	770	1034	264	/	0.49	14
TTQ-F-PEG (H2O)	792	1073	281	/	/	11
TTQ-TC (THF)	796	1042	246	21115	18.3	15
DPBTA-DPTQ NPs	817	1125	308	/	0.45	16
DHTDP NP	840	1050	210	/	/	17
DTP-DPTQ NPs	852	1120	268	/	0.01	18
O-T NPs	857	/	/	15500	0.038	19
O-BT NPs	845	1056	211	36500	0.35	20
TEEITQ NPs	855	1102	247	/	0.26	21
TTQ-SA (Toluene)	633	752	119	/	19.7	22
TP-TQ1 NPs	877	1032	155	16175	0.69	23
TP-OH NPs	843	1092	186	29077	1.05	**This work**

[a] $\lambda_{abs,max}$ is peak of maximum absorption; [b] $\lambda_{em,max}$ is peak of maximum emission; [c] ε is molar extinction coefficient; [d] quantum yield.

References

1. F. Neese, Software update: The ORCA program system—Version 5.0, *Wiley Interdiscip. Rev.: Comput. Mol. Sci.*, 2022, 12, e1606.
2. S. Grimme, S. Ehrlich, L. Goerigk, Effect of the damping function in dispersion corrected density functional theory, *J. Comput. Chem.*, 2011, **32**, 1456−1465.
3. T. Lu, F. Chen, Multiwfn: A multifunctional wavefunction analyzer, *J. Comput. Chem.*, 2011, **33**, 580–592.
4. W. Humphrey, A. Dalke, K. Schulten, VMD: Visual molecular dynamics, *J. Mol. Graphics*, 1996, **14**, 33—38.
5. J. Qi, C. Sun, A. Zebibula, H. Zhang, R. T. K. Kwok, X. Zhao, W. Xi, J. W. Y. Lam, J. Qian and B. Z. Tang, Real-Time and High-Resolution Bioimaging with Bright Aggregation-Induced Emission Dots in Short-Wave Infrared Region, *Adv. Mater.*, 2018, **30**, 1706856.
6. Li, C. Yin, R. Wang, Q. Fan, W. Wu and X. Jiang, Second Near-Infrared Aggregation-Induced Emission Fluorophores with Phenothiazine Derivatives as the Donor and 6,7-Diphenyl-[1,2,5]Thiadiazolo[3,4-g]Quinoxaline as the Acceptor for In Vivo Imaging, *ACS Appl. Mater. Interfaces*, 2020, **12**, 20281—20286.
7. S. Li, T. Cheng, C. Yin, S. Zhou, Q. Fan, W. Wu and X. Jiang, Phenothiazine versus Phenoxazine: Structural Effects on the Photophysical Properties of NIR-II AIE Fluorophores, *ACS Appl. Mater. Interfaces*, 2020, **12**, 43466—43473.
8. Y. Li, M. Zha, G. Yang, S. Wang, J.-S. Ni and K. Li, NIR-II Fluorescent Brightness Promoted by "Ring Fusion" for the Detection of Intestinal Inflammation, *Chem. – Eur. J.*, 2021, **27**, 13085—13091.
9. Y. Qin, X. Li, S. Lu, M. Kang, Z. Zhang, Y. Gui, X. Li, D. Wang and B. Z. Tang, Modular Construction of AIE-Active Supramolecular Cages with Tunable Fluorescence for NIR-II Blood Vessel Imaging, *ACS Mater. Lett.*, 2023, **5**, 1982—1991.
10. Y. Li, M. Zha, T. Kang, C. Li, X. Wu, S. Wang, S.-B. Lu, Y.-S. Lee, Y.-R. Wu, J.-S. Ni and K. Li, Promoted NIR-II Fluorescence by Heteroatom-Inserted Rigid-Planar Cores for Monitoring Cell Therapy of Acute Lung Injury, *Small*, 2022, **18**, 2105362.
11. K. He, S. Chen, Y. Chen, J. Li, P. Sun, X. Lu, Q. Fan and W. Huang, Water-Soluble Donor–Acceptor–Donor-Based Fluorophore for High-Resolution NIR-II Fluorescence Imaging Applications, *ACS Appl. Polym. Mater.*, 2021, **3**, 3238-3246.
12. K. He, S. Chen, W. Xu, X. Tai, Y. Chen, P. Sun, Q. Fan and W. Huang, High-stability NIR-II fluorescence polymer synthesized by atom transfer radical polymerization for application in high-resolution NIR-II imaging, *Biomater. Sci.*, 2021, **9**, 6434—6443.
13. Y. Li, X. Fan, Y. Li, S. Liu, C. Chuah, Y. Tang, R. T. K. Kwok, J. W. Y. Lam, X. Lu, J. Qian and B. Z. Tang, Molecular Crystal Engineering of Organic Chromophores for NIR-II Fluorescence Quantification of Cerebrovascular Function, *ACS Nano*, 2022, **16**, 3323—3331.
14. A. Ji, H. Lou, C. Qu, W. Lu, Y. Hao, J. Li, Y. Wu, T. Chang, H. Chen and Z. Cheng, Acceptor engineering for NIR-II dyes with high photochemical and biomedical performance, *Nat. Commun.*, 2022, **13**, 3815.
15. S. Chen, B. Sun, H. Miao, G. Wang, P. Sun, J. Li, W. Wang, Q. Fan and W. Huang, NIR-II Dye-Based Multifunctional Telechelic Glycopolymers for NIR-IIa Fluorescence Imaging-Guided Stimuli-Responsive Chemo-Photothermal Combination Therapy, *ACS Mater. Lett.*, 2020, **2**, 174—183.
16. D. Yan, W. Xie, J. Zhang, L. Wang, D. Wang and B. Z. Tang, Donor/π-Bridge Manipulation for Constructing a Stable NIR-II Aggregation-Induced Emission Luminogen with Balanced Phototheranostic Performance**, *Angew. Chem., Int. Ed.*, 2021, **60**, 26769—26776.
17. J. Cui, F. Zhang, D. Yan, T. Han, L. Wang, D. Wang and B. Z. Tang, "Trojan Horse" Phototheranostics: Fine-Engineering NIR-II AIEgen Camouflaged by Cancer Cell Membrane for Homologous-Targeting Multimodal Imaging-Guided Phototherapy, *Adv. Mater.*, 2023, **35**, 2302639.
18. P. Xiao, Y. Sun, M. Liang, S. Yang, J. Li, L. e. Zhang, X. Jiang and W. Wu, A fluorophore with dithienopyrrole donor for beyond 1300 nm NIR-II fluorescence/photoacoustic dual-model imaging and photothermal therapy, *Mater. Today Nano*, 2023, **24**, 100404.
19. J. Liu, Y. Xiong, Y. Gao, X. Xu, K. Chen, Q. Shen, W. Huang, Q. Fan and Q. Wang, Molecular Oligomerization and Donor Engineering Strategies for Achieving Superior NIR-II Fluorescence Imaging and Thermotherapy under 1064 nm Laser Irradiation, *Small*, 2023, **19**, 2205640.
20. Q. Wang, J. Liu, X. Zhang, Y. Tang, Y. Xiong, L. Zhang, T. Xiao and Q. Fan, *Chem. Commun.*, 2023, 59, 9611-9614.
21. J. Li, N. Niu, D. Wang, J. Zhu, X. Li, Q. Kong, B. Z. Tang and D. Wang, As Aggregation-Induced Emission Meets with Noncovalent Conformational Locks: Subtly Regulating NIR-II Molecules for Multimodal Imaging-Navigated Synergistic Therapies, *Angew. Chem., Int. Ed.*, 2025, **64**, e202413219.
22. Y. Chen, S.-Y. Yang, X. Ou, H. Wang, F.-C Kong, P. C. Y. Chow, Y. Wang, Y. Jiang, W. Zhao, J. Sun, R. T. K. Kwok, D.-W. Zheng, W. Yu, F. Wang, J. W. Y. Lam and B. Z. Tang, Engineering a Near-Infrared Spiro-Based Aggregation-Induced Emission Luminogen for DNAzyme-Sensitized Photothermal Therapy with High Efficiency and Accuracy, *J. Am. Chem. Soc.*, 2024, **146**, 35462—35477.
23. L. Zheng, Z. Zhao, C. Xue, L. An, W. Na, F. Gao, J. Shao and C. Ou, Planar-structured thiadiazoloquinoxaline-based NIR-II dye for tumor phototheranostics, *J. Mater. Chem. B*, 2024, **12**, 4197—4207.